Draft version May 23, 2012
Preprint typeset using LaTeX style emulateapj v. 11/10/09

FULL SURFACE AUTOMATED CORONAL HOLE DETECTION AND CHARACTERIZATION TO CONSTRAIN GLOBAL MAGNETIC FIELD MODELS

C. Lowder, J. Qiu, R. Leamon
Department of Physics, Montana State University, Bozeman, Montana 59717

and

Y. Liu
W. W. Hansen Experimental Physics Laboratory, Stanford University, Stanford, CA 94305

Draft version May 23, 2012

ABSTRACT

One of the primary mission goals of the Solar Terrestrial Relations Observatory (STEREO) : Extreme Ultraviolet Imager (EUVI) is to provide full extreme-ultraviolet (EUV) coverage of the solar surface in conjunction with the Solar and Heliospheric Observatory (SOHO) : Extreme Ultraviolet Imaging Telescope (EIT) or the Solar Dynamics Observatory (SDO) : Atmospheric Imaging Assembly (AIA). Now, five years after launch, sufficient orbital separation has occurred for this to come to fruition. Using EUV images from STEREO:EUVI in 195Å and SDO:AIA in 193Å, we can create full surface maps of coronal holes. Our method employs an intensity thresholding technique in conjunction with line-of-sight magnetic field measurements to automatically distinguish filament channels. This full surface coverage provides a unique opportunity to compare observed coronal holes with the predicted open magnetic field regions from both potential field models in addition to non-potential models. Our method is able to detect and characterize both long-term coronal hole structures, as well as shorter lived, transient coronal holes. Here, this method is described in detail, with comparisons drawn between observed coronal hole boundaries and open-field boundaries derived from models. In addition, quantities that are crucially dependent on these boundaries are considered, namely the open magnetic flux.

Subject headings: Sun: corona, Sun: magnetic topology

1. INTRODUCTION

Coronal holes are observationally a region of diminished emission in the extreme ultraviolet (EUV) and X-ray wavelengths, as compared to the quiet sun background level. One fundamental area of debate focuses on whether or not these coronal hole regions are necessarily tied to regions of open magnetic field. The field lines in these open regions are considered to be open to the heliosphere.

Some of the earliest observations linked these on-disk features with emission in EUV wavelengths. Tousey et al. (1968) noted from rocket observations that polar emission in EUV seemed weaker than in surrounding regions. More detailed observations were made possible by instruments onboard Skylab (Huber et al. 1974).

These open field regions are most often associated with long-lived coronal hole structures, which exist for days or months. However, there are instances of regions of depleted EUV emission that evolve rapidly in comparison, expanding and refilling in a matter of hours. These transient coronal holes, or coronal dimmings, are most likely associated with a depletion of coronal material following a coronal mass ejection (CME) which is magnetically anchored in this region. (Rust 1983; Thompson et al. 2000; Yang et al. 2008; Aschwanden et al. 2009)

A more detailed overview of the properties of coronal holes has been reviewed by Cranmer (2009).

The observational goal behind this research is to provide continuous, consistent, full solar surface observations of coronal hole boundaries. Current techniques exist which define these boundaries using synoptic maps from a single instrument. By combining the viewpoint of Solar Dynamics Observatory Atmospheric Imaging Assembly (SDO:AIA) with the Solar Terrestrial Relations Observatory Extreme Ultraviolet Imager (STEREO:EUVI A/B), full solar surface observations will be available for the next few years as the twin STEREO spacecraft continue to move with respect to the Earth.

Particular models of magnetic field reconstruction use coronal hole boundaries as a method of comparison with predicted open field regions. These observations can then provide a better constraint on the model boundary conditions and subsequent evolution. By providing full surface, realtime maps of coronal hole boundaries a better diagnostic tool for these models can be provided. In addition, comparison of observation with simulated global field results will motivate the need for more robust modeling tools.

2. METHODOLOGY

2.1. *Instrumentation*

Table 1 displays the availability of each dataset in use. Of particular importance is the overlap of sources of radial magnetic field from synoptic charts (SOHO:MDI and SDO:HMI) with sources of coronal hole boundaries (SOHO:EIT, SDO:AIA, STEREO-EUVI). A vast amount of data is available from the longer-lived SOHO mission, which will be clearly evident from the analysis to come.

The brief overlap between the EIT and AIA-EUVI datasets will serve as a crucial comparison between the two sources. The nature of the AIA-EUVI observations are slightly different in scope than those from EIT, and this will serve as a validation of the technique for all sets of instruments.

2.2. *Thresholding routine*

Building on the work of Krista & Gallagher (2009), I've developed an enhanced routine for automated coronal hole

clowder@solar.physics.montana.edu

TABLE 1
DATA COVERAGE FOR EACH INSTRUMENT SOURCE

		Start		End	
Source	Observable	CR	Date	CR	Date
SOHO:EIT	EUV 195Å	1909.96	1996 05 31	2105.27	2010 12 31
SDO:AIA	EUV 193Å	2096.76	2010 05 13	2118.72	2012 01 02
STEREO-EUVI	EUV 195Å	2096.76	2010 05 13	2118.72	2012 01 02
WSO Harmonic Coefficients	Radial magnetic field	1893.00	1995 02 23	2113.00	2011 07 29
SOHO:MDI Synoptic Charts	Radial magnetic field	1911.00	1996 06 28	2104.00	2010 11 26
SDO:HMI Synoptic Charts	Radial magnetic field	2096.00	2010 04 22	2120.00	2012 02 05

detection, capable of working with multiple input sources of data. Utilizing synoptic maps of derived radial magnetic field, this routine is able to distinguish between coronal holes (dominated by one magnetic polarity) and filaments (mixed polarity).

Each field of view image is processed using standard SSWIDL software routines for each particular instrument. The AIA images are read into memory and processed using `read_sdo.pro` and `aia_prep.pro`, respectively. The EUVI:A/B images are read and processed using the `secchi_prep.pro` routine. A mask is applied to each respective image to remove off-limb information. Each of the three processed and cropped images are then subdivided into eight sub-arrays. Figure 1 illustrates this sub-array arrangement.

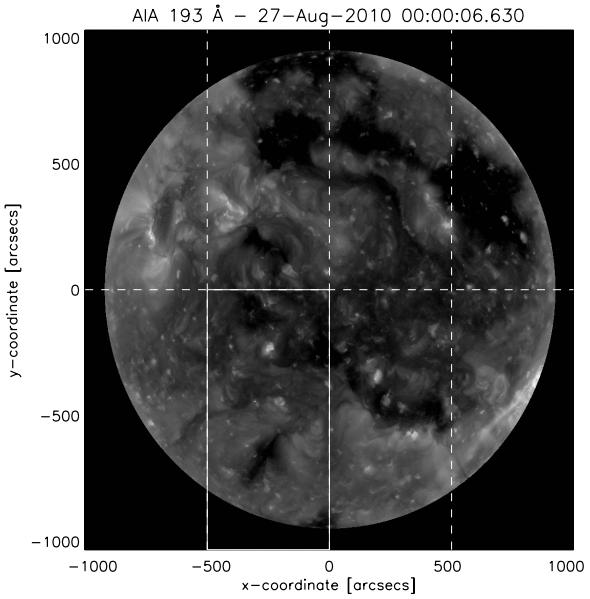

FIG. 1.— Full-disk EUV data taken at 193Å by the AIA instrument aboard SDO. The thresholding routine proceeds to partition this data into eight sub-arrays, on each of which the code runs the thresholding calculation. Each sub-array contains a differing mixture of bright and dark features. The solid boxed sub-array marks the sub-array being considered in Figure 2.

Gallagher et al. (1998) have shown that a histogram of EUV intensity corresponds to the contribution from multiple sources. More importantly, by thresholding an image in the valley between contributing peaks in EUV intensity histograms, features can be separated. The justification for partitioning an image into sub-arrays is two fold. The first reasoning is to avoid any bad blocks or missing portions of an image array. The second reasoning involves the thresholding intensity located in the valley between contributing peaks. Consider a histogram of EUV intensity, measured in DN, as displayed in Figure 2. The EUV intensity histograms of the full field of view, and the sub-array marked in Figure 1 are displayed in the solid curve and dashed curve, respectively. Each curve is normalized for comparison.

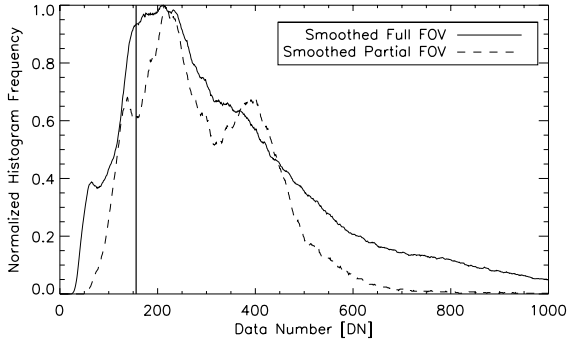

FIG. 2.— Histogram of the sub-array marked in Figure 1, calculated in terms of data number for the recorded image. This figure displays a limited range of the full extent of the data, and has been boxcar smoothed with a width of 10 DN for clarity of the underlying form of the data. The solid curve and dashed curve refer to the full field of view, and the marked subarray, respectively. The vertical line indicates the local minimum value that is appropriate as a thresholding value in DN. Note that this local minimum is not readily detectable in the full field of view data.

Various contributing sources combine to create the full histogram profile as seen. The particular contributions for this study are the lower emission coronal hole regions, and the brighter quiet sun regions. For the sub-array field of view pictured, these peak at 140 DN and 220 DN, respectively. The local minimum between these two peaks defines the threshold between these two features. The full field of view histogram does not clearly display this local minimum, due to overlap with contributions from many more sources. By partitioning the image into sub-arrays, the overlap from other sources is minimized. In addition, the shape of each sub-array is vertical in nature to better capture contribution from both polar coronal holes and quiet regions.

An EUV intensity histogram is calculated for each sub-array, and this local minimum is computed using a number of logic tests. After each value is computed, those that lie outside the range of possibility are discarded, and a full field of view thresholding value is computed from the mean of the valid sub-array values. This full field of view value is then used to partition the array.

This code was then tested with and used to gather results from several instruments. Despite using multiple instruments

with differing calibrations, this modified routine has proven consistent with maintaining stable coronal hole thresholding values as well as coronal hole boundaries, even between instruments. Consider Figure 3, which displays the thresholding value for each of the three instruments being used in the full surface observations, SDO:AIA, STEREO A:EUVI, and STEREO B:EUVI. The values are displayed as a ratio with the quiet sun value, to avoid dimensionality. Quiet sun values were determined through the median data number within each frame. This ratio value stays relatively stable throughout the dataset shown, a significant portion of the data availability of AIA at the time of writing. There are, however, variations in this ratio over time, which highlights the requirement for a dynamic nature to the threshold value. The program is scalable to multiple cadence values depending on the particular data set being analyzed. For persistent coronal holes, one day cadence is appropriately manageable. To study transient coronal holes, the cadence is limited only by the instrument and available disk space.

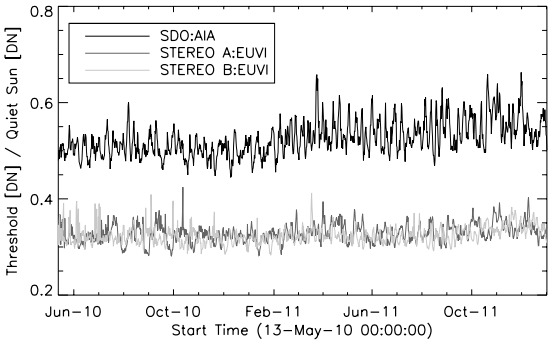

FIG. 3.— Ratio of the data number thresholding value as a ratio of the quiet sun value for each instrument employed in full solar surface observations.

In addition to the full surface observations made possible by the AIA and EUVI instruments, earlier observations are available from the SOHO:EIT instrument. With EIT, the view is limited to one vantage point, however, there are far more data available. This enables much longer-term studies of this thresholding routine, as well as coronal hole detection. Figure 4 illustrates a similar ratio of threshold value to quiet sun over the course of EIT observations available. Variations are present in this ratio, as are gaps in the data. Over this much longer time range, the importance of a dynamic thresholding ratio is clearly apparent.

2.3. *Coronal hole determination*

As mentioned previously, one of the benefits of using a combination of data sources from AIA and EUVI A/B is the ability to have near full surface observations. For the example observation provided, 2010 August 27 00:00:00 UT, the two STEREO spacecraft have separated in their orbits to provide a nearly full surface view. Areas with a complete lack of coverage do exist, but are not of crucial concern for this example. Several months later, full coverage was achieved by the three spacecraft, and this complete coverage will continue for several years to come. Figure 5 displays the coverage overlap between the three instruments. Dark areas indicate a complete lack of coverage, with increasing brightness indicating instrument overlap. AIA, EUVI:A, and EUVI:B are centered at Carrington longitude 130, 215, and 40 degrees, respectively.

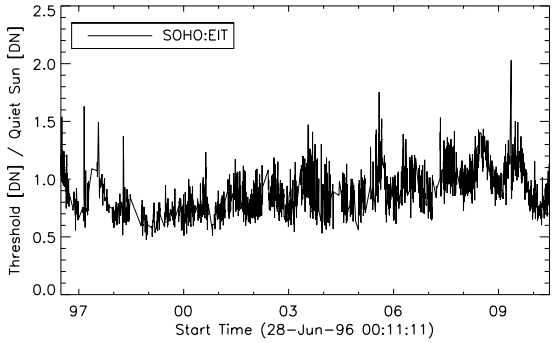

FIG. 4.— Ratio of the data number thresholding value as a ratio of the quiet sun value for the EIT instrument on board SOHO.

With the thresholding on each instrument completed for a particular time frame, each array is converted into a boolean array, with 0 indicating regions above the threshold value for that instrument at that particular time. A value of 1 in a pixel marks areas below the threshold value. These individual arrays are then projected into a Carrington equal area map, marked in longitude and sine latitude. In addition to the criteria of EUV intensity, a coronal hole candidate region must also tend towards a dominating polarity. Coronal hole regions are most often clearly dominated by a single magnetic polarity over their entire area (Wang 2009). Filament channels are characterized by depleted intensity in EUV wavelengths, similar to coronal holes. However, filament channels lie along a polarity inversion line, and thus lie atop a region which will tend to be neutral magnetic polarity. Each of the suspect regions are overlaid with an HMI synoptic map of radial magnetic field, as displayed in Figure 6. For each region in question composed of N pixels, there exist N values of magnetic flux, defined as ϕ. We can define the skew of the magnetic flux as, denoting it as the variable γ,

$$\gamma = \frac{1}{N}\sum_{j=0}^{N-1}\left(\frac{\phi_j - \bar{\phi}}{\sigma}\right)^3 \quad (1)$$

Here $\bar{\phi}$ denotes the mean flux value within a particular region and σ denotes the standard deviation of the flux values within the region. The value of magnetic flux skew is calculated for each suspected coronal hole region in this way. Figure 7 displays the skewness value for each of the suspected regions, scaled relative to one another. The background grey value indicates zero skew, with each region scaled with respect to one another. Darker regions indicate a skew towards negative magnetic flux, while lighter regions indicate a skew towards positive magnetic flux. Contours have been drawn around regions whose magnetic flux skew exceed 0.5 in magnitude, the criteria used for coronal hole labeling.

Note that the filament channel region labeled in Figure 6 has a skew close to zero, and is not contoured. Magnetic flux histograms are compared for the labeled coronal hole and filament channel in Figure 8. The histogram of magnetic flux in the filament channel shows a relative balance between positive and negative magnetic flux. The histogram for the magnetic flux in the coronal hole, however, is noticeably skewed towards negative magnetic flux values. The magnetic flux skew values in the coronal hole and filament channel regions are -7.52326 and 0.341194, respectively.

Figure 9 displays a histogram of the magnetic flux skew

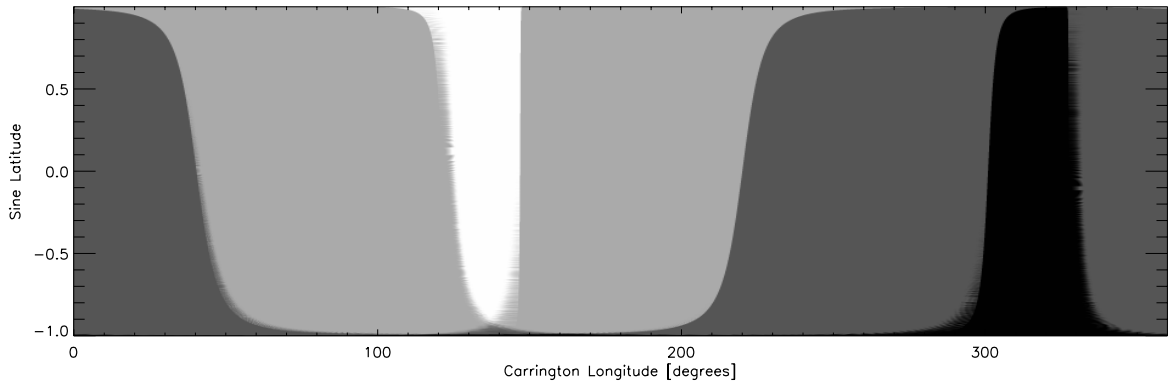

FIG. 5.— Available instrument coverage for the particular date under consideration. Dark regions indicate a complete lack of coverage, while increasing brightness indicates instrumental coverage and overlap. The field of view for AIA, EUVI:A, and EUVI:B are centered at Carrington longitude values of 130, 215, and 40 degrees, respectively.

values for each of the suspected coronal hole regions. Vertical dashed lines display the cutoff value of ±0.5.

2.4. *Persistence of coronal holes*

For a given dataset, each individual set of data frames is characterized by a discretized set of spatial and temporal coordinates, a set of colatitudes, longitudes, and time frames, $\{\theta, \phi, t\}$. This set is discretized such that each is indexed by a integer value, $\{\theta_i, \phi_j, t_k\}$. For each of these values, a byte value is assigned that indicates the presence of a coronal hole, defined as a scalar function, $\psi(\theta_i, \phi_j, t_k)$. For a particular range of time, a 'persistence map' can be defined as the overall persistence of a coronal hole within a particular location. This map can be defined as,

$$\Psi(\theta_i, \phi_j) = \sum_k \psi(\theta_i, \phi_j, t_k) \quad (2)$$

This persistence map will give a visual comparison as to the persistence of each coronal hole region, compared through multiple instruments.

3. PERSISTENT CORONAL HOLES

3.1. *EIT database*

Following a similar line of reasoning as McIntosh et al. McIntosh (2009), we use the Fe XII emission as measured by the Extreme Ultraviolet Imaging Telescope (EIT) onboard the Solar and Heliospheric Observatory (SOHO). This routine was applied to the entire EIT dataset in 195Å. This dataset spans back to 1996, capturing the entire variation along a solar cycle. This provides a unique opportunity to consistently study persistent coronal holes throughout the activity variation of a solar cycle.

Figure 10 illustrates one output of this routine, a persistence map of the coronal hole distribution throughout this time period. These persistence maps illustrate for a particular latitude and longitude position on the solar surface, the persistence of a coronal hole in this location measured in days. Each detected coronal hole has been projected into a Carrington map, and aligned with each following frame. The dataset in consideration spans Carrington rotation 1920-2098, at a cadence of one frame per day. The persistence map illustrates the overall distribution pattern and persistence of each hole.

As one would expect, the majority of coronal hole persistence occurs near the polar regions, with more sparsely populated lower latitude regions.

3.2. *AIA-EUVI full surface maps*

The EIT instrument onboard SOHO is limited to the view from Earth, leaving a major portion of the solar surface uncovered. Complete coverage is crucial for understanding the dynamics of long-term coronal hole evolution. STEREO:EUVI provides a comparable dataset to that used on EIT, with the added bonus of multiple viewpoints.

In conjunction with the recently launched SDO:AIA, these instruments will provide full surface coverage for the next few years. This will provide a unique look at the properties of coronal holes as the next solar cycle ramps up.

I employ AIA 193Å data, capturing emission in Fe XII and XXIV. In addition, EUVI 195Å data is used, looking at the Fe XII emission. Each dataset is sampled at 24 hour cadence. In addition, the line of sight magnetic field is recorded using data from the Helioseismic and Magnetic Imager (HMI) onboard SDO. This dataset is sampled at the same cadence as the EUV images, providing the line of sight magnetic field from the SDO view angle for filament detection.

Figure 11 displays a persistence map for the AIA-EUVI dataset, from Carrington rotations 2096-2113. Darker areas contain pixels with a longer-persisting coronal hole during the time period indicated. Note that this persistency is not continuous in nature, but totaled over the entire period under consideration. Polar coronal holes exist as the most persistent feature. Lower latitude features exist and persist as well. These patterns of persistency will be compared with magnetic field extrapolation models, described in the following section. An online animation is linked to within the Figure 11 caption, which illustrates the frame-by-frame building process of the persistency map. This animation also sheds light on the temporal evolution of these open regions.

This persistency profile can be compressed along longitude values, to yield a profile for coronal hole persistency as a function of latitude. Figure 12 displays the latitude persistency profile for the AIA-EUVI surface maps.

In addition to describing the coronal holes in terms of persistency, we can also consider other properties of these holes over a long period. Figure 13 displays the coronal hole area, as well as the unsigned open magnetic flux determined from these coronal hole boundaries in conjunction with radial magnetic field synoptic charts from SDO:HMI. During the time range studied, coronal holes covered roughly 0.05-0.10 of the

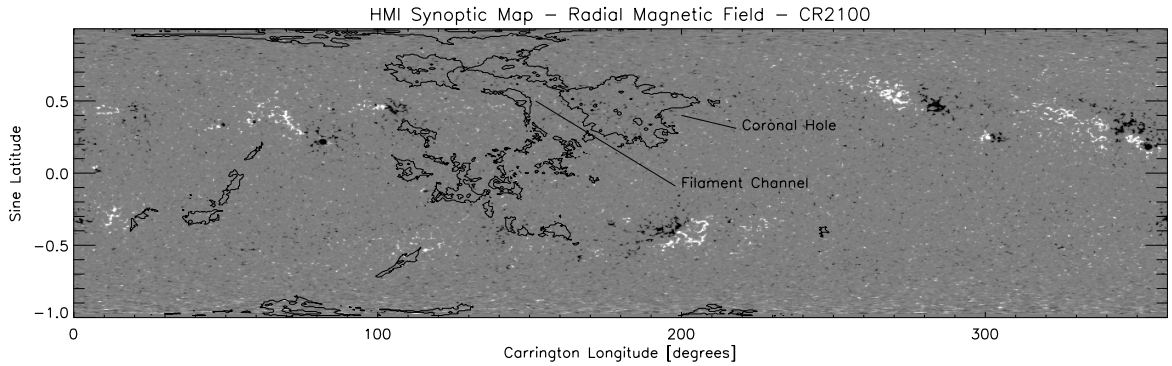

FIG. 6.— HMI synoptic map of radial magnetic field for Carrington rotation 2100, with contours of initially suspected coronal hole regions. Each source of data, AIA and EUVI A/B, were run through the thresholding routine, producing a DN threshold value for each source. Contours were produced of regions below this thresholding value, and projected into a Carrington equal area projection.

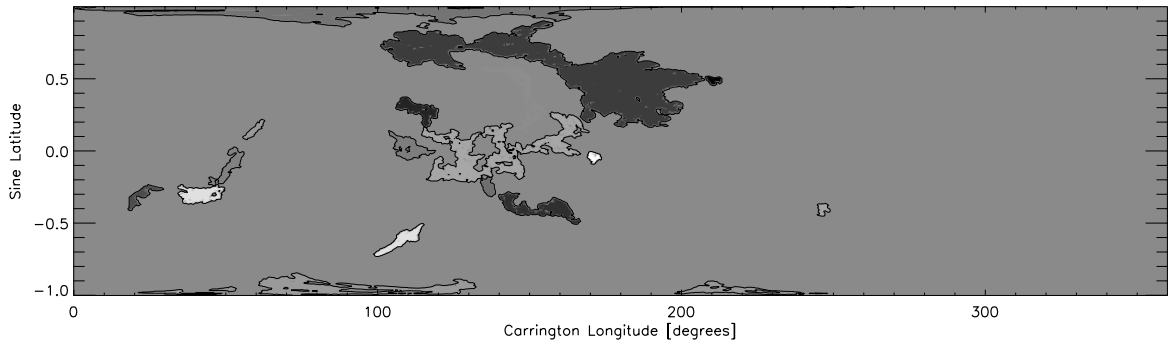

FIG. 7.— Partitioned suspected coronal hole regions, displayed with color indicating the relative magnetic flux skew value within that region. Magnetic flux values were obtained through overlap with the HMI synoptic map of radial magnetic field. Grey indicates low magnitude skew values, where positive and negative flux are relatively equally distributed. Regions dominated by positive or negative magnetic flux are indicated through white or black shading, respectively. Contours have been applied to those regions with a magnetic flux skew magnitude greater than 0.5.

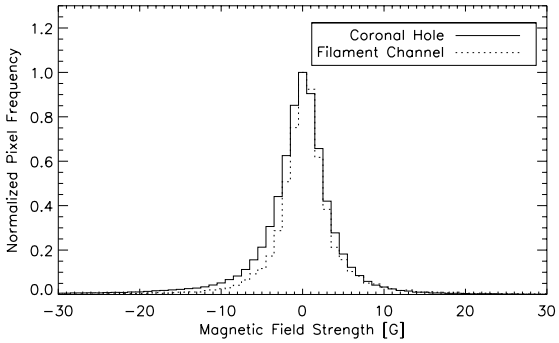

FIG. 8.— Example of the magnetic flux distribution within two suspected coronal hole regions. The solid line displays a histogram of magnetic flux for a positively identified coronal hole region. The flux is slightly off balance, tending toward negative polarity. The dashed curve is data from an identified filament channel, which is more balanced in flux distribution. The calculated skew values for this coronal hole and filament channel are -7.52326 and 0.341194, respectively.

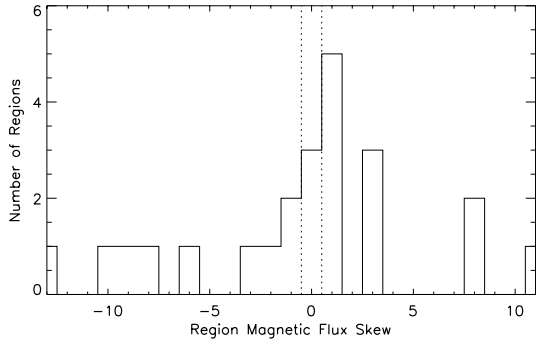

FIG. 9.— Histogram of the calculated magnetic flux skew values for the particular time frame under consideration. Vertical dashed lines indicate the magnetic flux skew cutoff value, 0.5. Regions whose calculated magnetic flux skew are less than 0.5 in magnitude are identified as filament channels.

total solar surface area. This value is in agreement with previous studies of coronal hole areas during the SOHO era (Harvey & Recely 2002).

3.3. *Preliminary model comparison*

The potential field source surface (PFSS) model is employed for this study to reconstruct the global coronal magnetic field. Using spherical harmonic coefficients from the Wilcox Solar Observatory, the magnetic field at the solar surface can be reconstructed. One of the major assumptions in this model is the lack of current below $2.5R_{\odot}$, which allows a magnetic scalar potential to be defined which satisfies,

$$\nabla^2 \Phi_M = 0 \tag{3}$$

Using the reconstructed magnetic field at the solar surface as one boundary condition, and the assumption that the field is purely radial at $2.5R_{\odot}$, this potential can be calculated within this region. From this potential, the field is then calculated as,

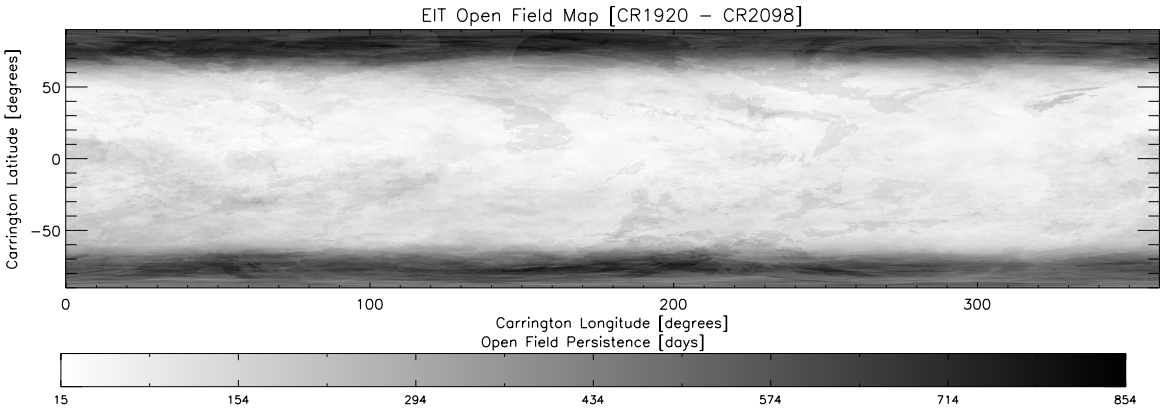

FIG. 10.— Coronal hole persistence map using the entire EIT 195Å database. Each pixel represents the total 'persistence' measured in days of a coronal hole within that pixel. Note that this persistency is not necessarily contiguous in time.

$$\mathbf{B} = -\nabla\Phi_M \tag{4}$$

As a first step in comparing these maps with reconstructed magnetic field data, an appropriate dataset was chosen and run through the algorithm. Figure 11 shows the coronal hole persistence for Carrington rotations 2096-2113, the entire available set of joint AIA and EUVI observations. For comparison, magnetic field spherical harmonic coefficients were obtained from the Wilcox Solar Observatory and reconstructed using a PFSS model. Although many approximations are involved, the reconstructed open field map matches quite closely with observations. Many features can be observed in both diagrams. The polar coronal holes are in agreement, with similar extent in latitude, even matching extent at different values of longitude. A central region of persistent holes can be observed centered around 180 degrees longitude, 10 degrees latitude. A similar structure of persistent holes will three regions of lower persistency can be observed in the open field reconstruction. A similar band of persistent holes extending upward from the southern polar hole region can be observed at 25 degrees longitude, -25 degrees latitude. A band of persistent holes can also be observed extending at 120 degrees longitude,

To further quantify the comparison, the persistence maps are projected into functions of latitude. Figure 12 illustrates this projection. Again, similar features are observed in both.

$$\lambda(\theta_i) = \sum_j \Psi(\theta_i, \phi_j) \tag{5}$$

Comparison with PFSS models shows that while some large scale features are preserved from observation to model, there are clearly discrepancies. We aim here to characterize the extent and nature of these disagreements, as a diagnostic tool to assess the viability of a PFSS reconstruction for a particular goal, most notably to characterize some of the model assumptions listed above.

3.4. *Open flux estimate*

In addition to the spatial hole data, magnetic flux measurements are available. Using the persistence information previously mentioned, the magnetic flux can be defined via,

$$\Phi_M(t_k) = R_\odot^2 \sum_{i,j} \psi(\theta_i, \phi_j, t_k) \cos(\theta_i) B_r(\theta_i, \phi_j, t_k) \tag{6}$$

We wish to compare several aspects of the magnetic flux, compared between multiple observational sources and models. For the time ranges available for consideration, Figure 14 displays the relative flux polarity within each time frame. In addition, each frame is broken into spatial regions. Here, the southern pole is defined for latitudes from -90 to -45 degrees, the low latitudes regions is defined from -45 to 45 degrees, and the northern pole is defined from 45 to 90 degrees. For the limited range of AIA-EUVI observations, it is clear that the southern pole is dominated by strong positive flux. In contrast, the northern pole is dominated by negative flux, however of much weaker magnitude. Low latitude regions are more mixed, with a slight tendency towards negative flux. The spread for these low latitude regions is much higher than the polar regions. The longer range of EIT observations yields a bit more insight into these magnetic flux properties. The polar regions undergo a flux reversal during these observations, which is evident from this figure. The northern pole is dominated by a strong positive magnetic flux at some points, and a weaker negative dominance at some other point. The southern pole shows the exact opposite trend, being dominated by strong negative magnetic flux at some points, and by weaker positive magnetic flux at others. Low latitude regions show a spread on both sides of the polarity.

Figure 15 displays the temporal evolution of these flux measurements. The top half of this figure displays the total signed open magnetic flux within each of the spatial regions as defined earlier. With some slight variations over time, the trends observed from Figure 14 still hold evident. The southern pole is dominated by strong positive flux, the northern pole is weakly dominated by negative flux, and the low latitudes are more mixed, with a slight tendency towards negative fluxes. Here, the time evolution is more evident, as the low latitude regions are mostly negative for the first nine months of observation, where they transition to positive dominance. This then reverses back and forth a few times. The bottom portion of this figure shows the total unsigned magnetic flux, also broken in spatial regions, as well as an overall measurement. The majority of the unsigned open flux resides within the southern and low-latitude regions, with the northern pole making a small contribution. This resonates well with Figure 11, which clearly shows both observation and reconstruction tending towards more persistent southern holes.

Figure 16 displays similar results using the EIT/MDI data. The top portion of this figure shows the total signed open magnetic flux, in comparison with the results from the top portion

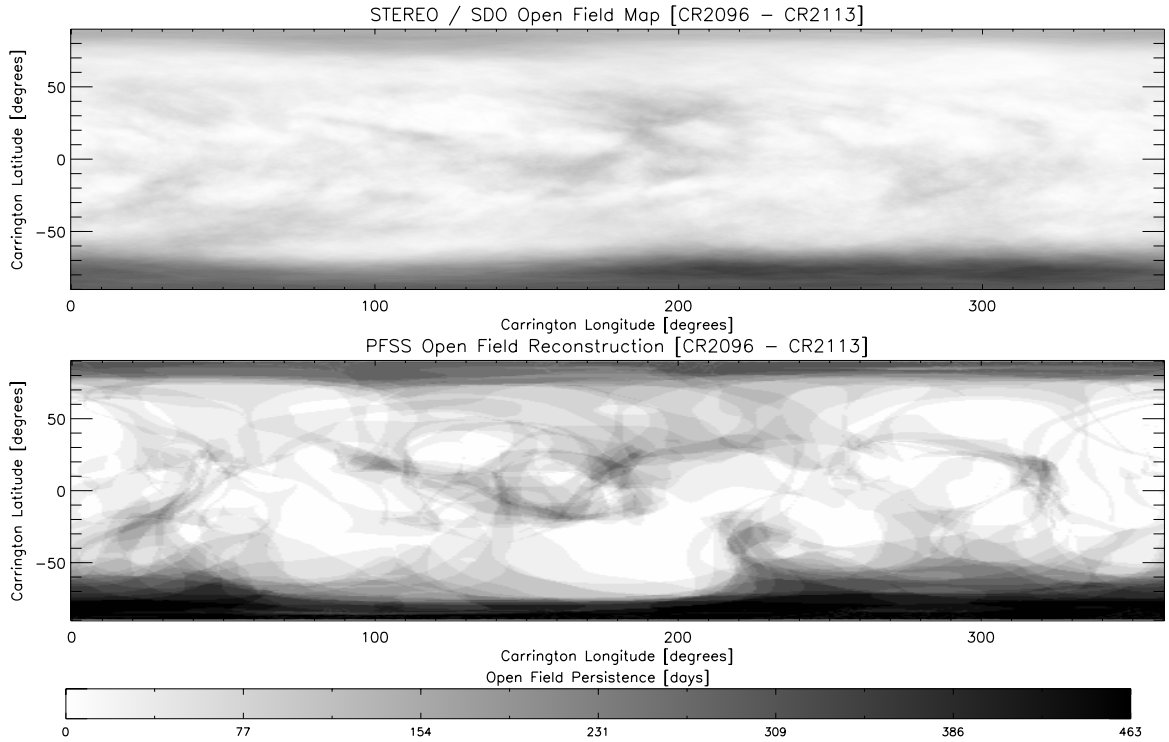

FIG. 11.— Coronal hole persistence map for a combination of AIA 193Å and EUVI 195Å datasets, along with a corresponding map generated using spherical harmonic coefficients obtained from the Wilcox Solar Observatory and a PFSS open field reconstruction. An animation illustrating the 'building' of the AIA-EUVI persistence map is located at http://solar.physics.montana.edu/clowder/movs/ch_map_build.mp4.

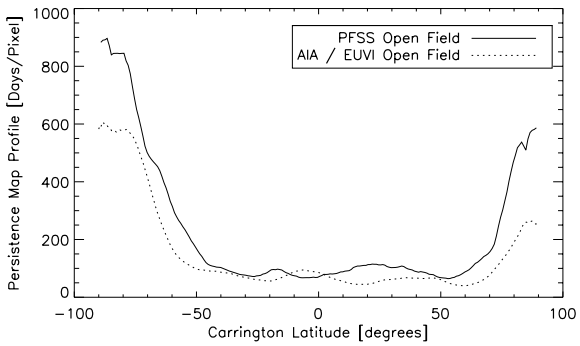

FIG. 12.— Coronal hole persistence map projected as a function of latitude. The two profiles are in units of *days/pixel*.

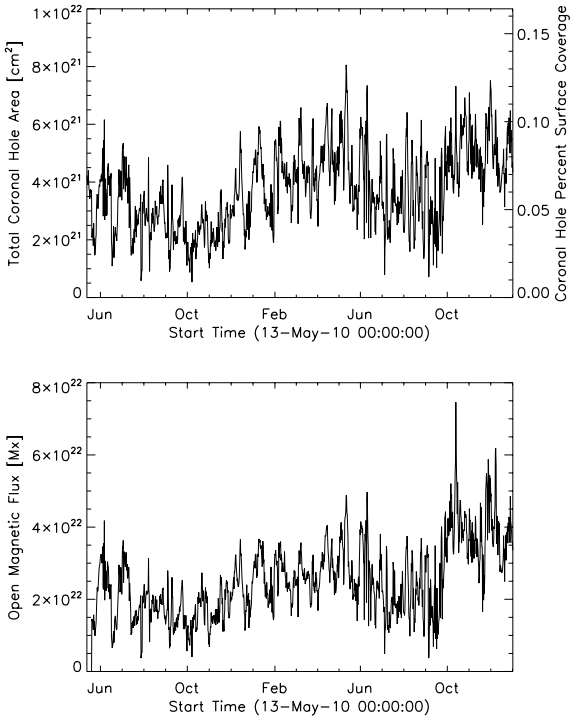

FIG. 13.— (a) Total coronal hole area over the time range captured by simultaneous AIA-EUVI observations. Fractional solar surface area coverage is also displayed. (b) Unsigned open magnetic flux as defined by coronal hole boundaries observed in simultaneous AIA-EUVI observations.

of Figure 15. Here, the temporal evolution of the previously mentioned flux reversal is evident. Whereas from 1996 until 2000 the northern pole is dominated by positive flux, and the southern pole dominated by negative flux, this trend reverses after 2000. Moreover, the overall magnitude of the signed flux indicates that the relative dominance of the respective polarities is much weaker after this reversal. Observations from AIA-EUVI maps have been displayed in dashed style. These values match well during the overlap with EIT. The bottom half of this figure shows the total unsigned magnetic flux. For comparison, total unsigned magnetic flux values were also calculated from the PFSS reconstruction of open magnetic field regions from WSO spherical harmonic coefficients. These values are displayed in purple. While the EIT observations seem to undershoot the PFSS calculations from roughly 1998 until 2003, the values are quite similar in mag-

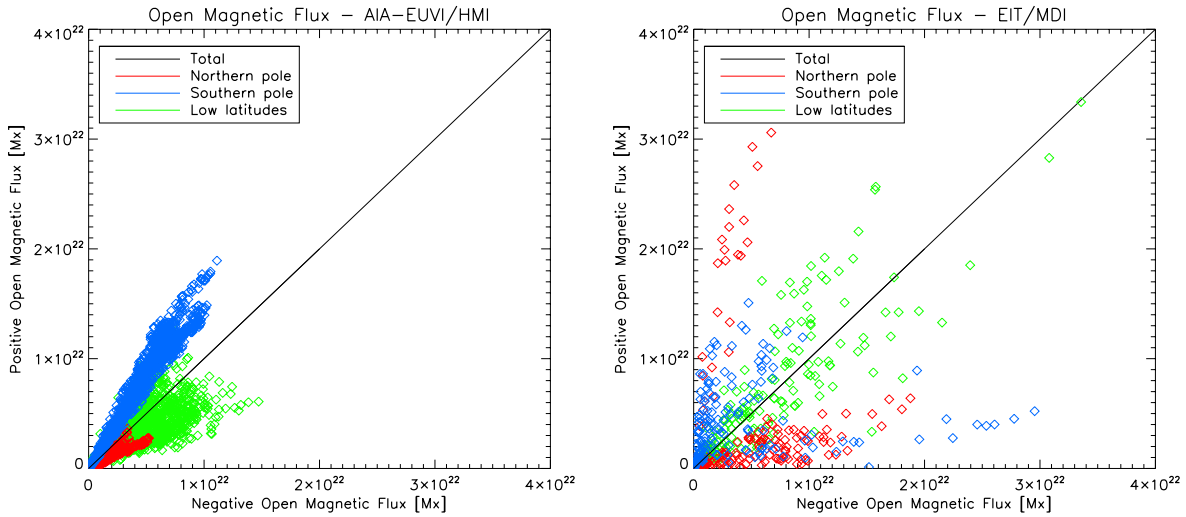

FIG. 14.— Scatter plot to illustrate the total flux balance within each timestep. Flux is subdivided into three segments depending on location. The southern polar, low-latitude, and northern polar regions extend between [-90,-45], [45,45], [45,90] degrees latitude respectively. The left subfigure displays the relative flux values from full-surface observations from AIA-EUVI, in conjunction with HMI synoptic charts. The right subfigure displays the relative flux values for the EIT observations in conjunction with MDI synoptic charts. Note that AIA-EUVI observations were conducted at 12 hour cadence, while EIT observations have been condensed to one data point per rotation.

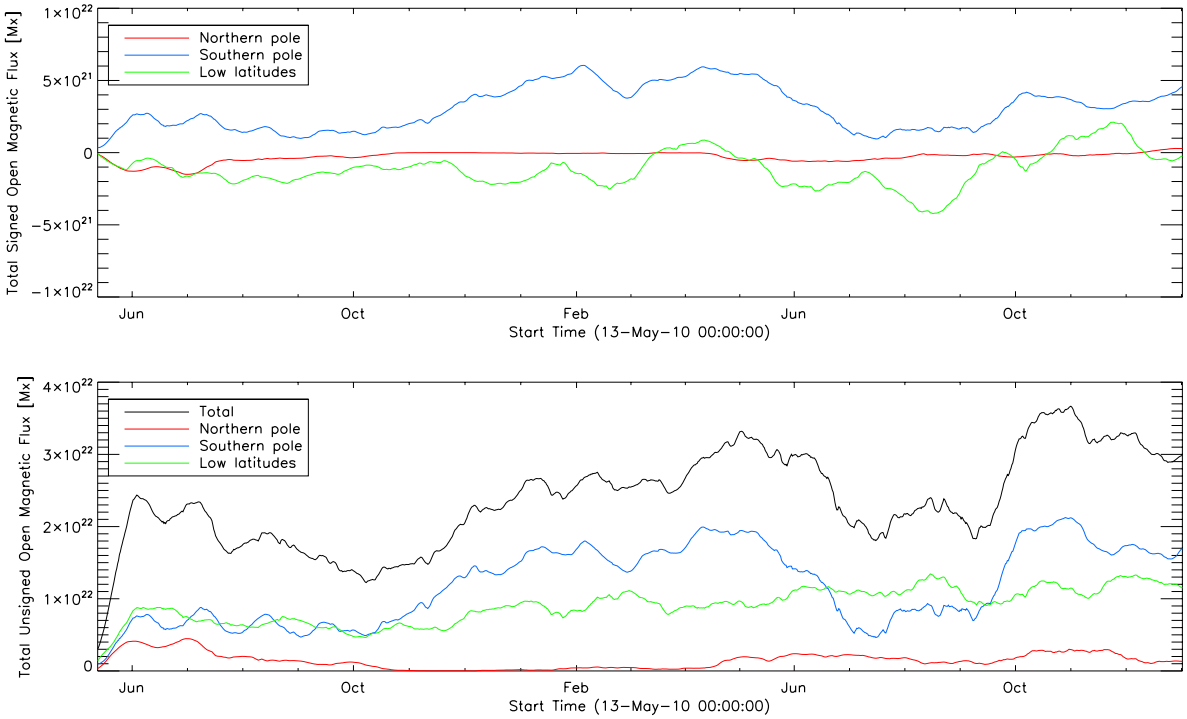

FIG. 15.— Signed and unsigned open magnetic flux from AIA-EUVI surface maps of coronal hole boundaries. Flux is subdivided into three segments depending on location. The southern polar, low-latitude, and northern polar regions extend between [-90,-45], [45,45], [45,90] degrees latitude respectively.

nitude from thereon. This undershooting is likely a consequence of the single vantage point of these EIT observations, which tends to underestimate the total coronal hole area during one rotation. AIA-EUVI observations of total unsigned open magnetic flux have been displayed in blue. These values match reasonably well with the overlap with EIT data, and show a clear rising in the total unsigned open magnetic flux.

One limitation of the full surface map is the partial magnetic field availability. The line of sight magnetic field measurements are only taken onboard the SDO spacecraft, and are therefore only for one vantage angle. However, if we assume that for the course of one rotation the relevant magnetic field does not drastically change in the coronal hole interior regions, a synoptic chart approach may be taken. Using synoptic charts obtained by HMI and MDI, open flux measurements can be obtained for each time frame under consideration. These open flux measurements compare well with model calculations and in situ observations (Yeates et al. 2010).

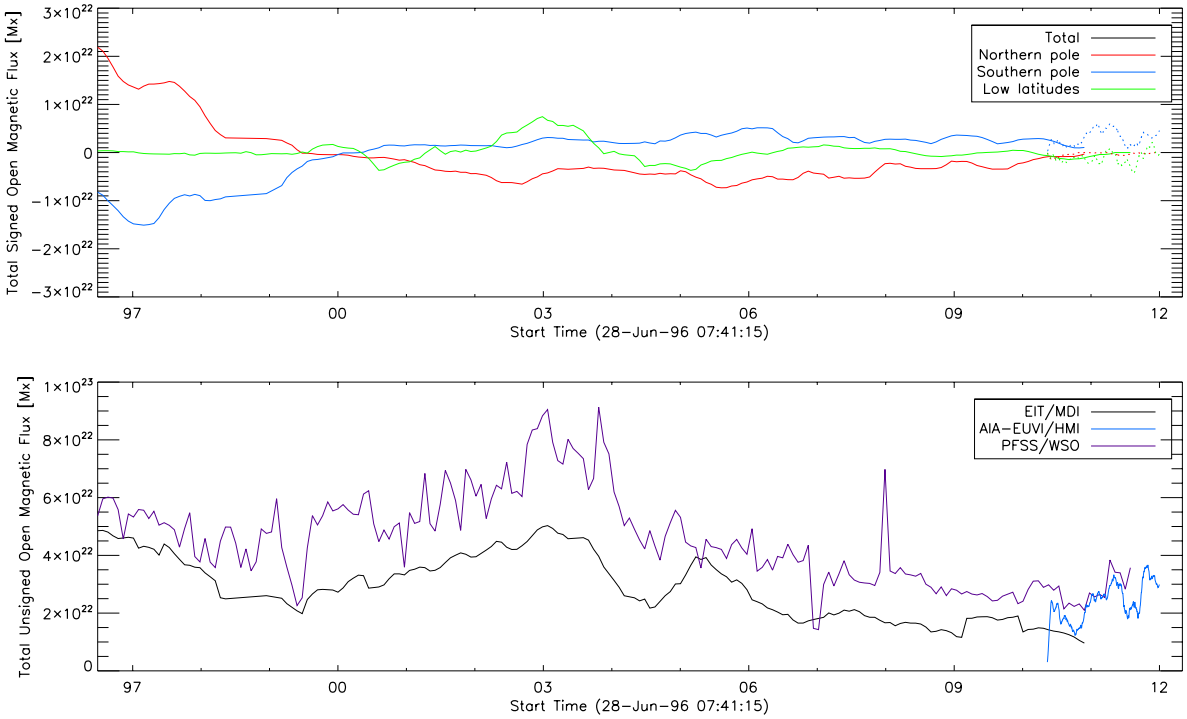

FIG. 16.— Signed and unsigned open magnetic flux from EIT surface maps of coronal hole boundaries. Flux is subdivided into three segments depending on location. The southern polar, low-latitude, and northern polar regions extend between [-90,-45], [45,45], [45,90] degrees latitude respectively. The lower subfigure displays the unsigned open flux values derived from PFSS reconstructions of open magnetic field from WSO harmonic coefficients. Unsigned open flux values from AIA-EUVI observations are displayed in conjunction with EIT observations.

4. CONCLUSIONS

Studies have been conducted previously to track the spatial and temporal evolution of coronal holes (Timothy et al. 1975; Miralles et al. 2001; McComas et al. 2002). This study involves a much broader time range of observations, in conjunction with a larger variety of instruments. The considerable overlap between observations speaks towards the reliability and application of this methodology.

Full surface observations will also allow a unique opportunity to better constrain the boundary conditions employed in magnetic field reconstruction models. Current observational constraints on these models rely on Earth-side observations, evolved forward in time when data is unavailable. Continuous observation of coronal hole boundaries will enhance model constraints, contributing to space weather prediction models.

There are a number of assumptions and limitations with the PFSS model. The model itself is static in nature, which pairs well with the high cadence observation of open field regions afforded by AIA-EUVI observations. In addition, the reconstruction is based on a 27-day average magnetic field map. The assumption that the field is potential in nature is another suspect assumption. The fixed surface at $2.5R_{\odot}$ is also a particular assumption that makes this model assuming in nature.

This motivates the need for the usage of non-potential models, which have several major advantages over potential models. Non-potential models include, inclusion of current within the corona, a dynamic nature, utilizing an evolving boundary condition, contrasted with the static nature of PFSS, and fewer limitations on the source surface at $2.5R_{\odot}$

By comparing coronal hole observations with both potential and non-potential models, insight into the limiting assumptions and model parameters can be gained. In particular, comparison will be made with the non-potential model developed by Yeates et al. (2010). This model is non-potential in nature, evolving the global magnetic field through a series of near force-free equilibria.

This code currently only considers the absolute boundaries of these coronal hole regions. No information is recorded containing information about the intensities located within each hole. This was mainly a problem given the issue of scattered EUV emission within the holes. While the boundaries could be defined relatively simply, interpreting the intensities within each hole proved inaccurate. Shearer et al. (2012) have worked on reducing the scattered light issue within these holes. This yields a more accurate EUV intensity within coronal hole regions, which opens up a whole new avenue of thought for this problem.

The importance of higher cadence observations is evident for observations of transient coronal holes, however, the expanded field of view is also crucial for understanding the global changes incurred by these dimmings. Miklenic et al. (2011) have studied the evolution of a coronal dimming taking advantage of the multiple viewpoints of the STEREO spacecraft. Future studies using the routines developed here will take full advantage of these multiple viewpoints.

Previous studies of transient coronal dimming have yielded some topological insight into the mechanics of solar eruptions. This new algorithm is easily scalable to this higher cadence analysis. This automated consistency should provide an enhanced understanding of how transient coronal dimmings are related to global magnetic field reconfiguration.

REFERENCES

Aschwanden, M. J., Nitta, N. V., Wuelser, J.-P., et al. 2009, The Astrophysical Journal, 706, 376

Cranmer, S. R. 2009, Living Reviews in Solar Physics, 6, 3

Gallagher, P. T., Phillips, K. J. H., Harra-Murnion, L. K., & Keenan, F. P. 1998, Astronomy and Astrophysics, 335, 733
Harvey, K. L., & Recely, F. 2002, Solar Physics, 211, 31
Huber, M. C. E., Foukal, P. V., Noyes, R. W., et al. 1974, Astrophysical Journal, 194, L115
Krista, L. D., & Gallagher, P. T. 2009, Solar Physics, 256, 87
McComas, D. J., Elliott, H. A., Gosling, J. T., et al. 2002, Geophysical Research Letters, 29, 4
McIntosh, S. W. 2009, The Astrophysical Journal, 693, 1306
Miklenic, C., Veronig, A. M., Temmer, M., Möstl, C., & Biernat, H. K. 2011, Solar Physics, 273, 125
Miralles, M. P., Cranmer, S. R., & Kohl, J. L. 2001, The Astrophysical Journal, 560, L193
Rust, D. M. 1983, (COSPAR, 34, 21
Shearer, P., Frazin, R. A., Hero, A. O. I., & Gilbert, A. C. 2012, The Astrophysical Journal Letters, 749, L8
Thompson, B. J., Cliver, E. W., Nitta, N., Delannée, C., & Delaboudinière, J.-P. 2000, Geophysical Research Letters, 27, 1431
Timothy, A. F., Krieger, A. S., & Vaiana, G. S. 1975, Solar Physics, 42, 135
Tousey, R., Sandlin, G., & Purcell, J. 1968, Structure and Development of Solar Active Regions, 35, 411
Wang, Y.-M. 2009, Space Science Reviews, 144, 383
Yang, L.-H., Jiang, Y.-C., & Ren, D.-B. 2008, Chinese Journal of Astronomy and Astrophysics, 8, 329
Yeates, A. R., Mackay, D. H., van Ballegooijen, A. A., & Constable, J. A. 2010, Journal of Geophysical Research, 115, 09112